AIP Advances

Hybrid electrochemical supercapacitor based on birnessite-type MnO_2/carbon composite as the positive electrode and carbonized iron-polyaniline/nickel graphene foam as a negative electrode

Cite as: AIP Advances **10**, 065113 (2020); https://doi.org/10.1063/5.0011862
Submitted: 27 April 2020 . Accepted: 21 May 2020 . Published Online: 08 June 2020

M. N. Rantho, M. J. Madito, K. O. Oyedotun, D. J. Tarimo, and N. Manyala

Hybrid electrochemical supercapacitor based on birnessite-type MnO_2/carbon composite as the positive electrode and carbonized iron-polyaniline/nickel graphene foam as a negative electrode

Cite as: AIP Advances 10, 065113 (2020); doi: 10.1063/5.0011862
Submitted: 27 April 2020 • Accepted: 21 May 2020 •
Published Online: 8 June 2020

M. N. Rantho, M. J. Madito, K. O. Oyedotun, D. J. Tarimo, and N. Manyala[a)]

AFFILIATIONS

Department of Physics, Institute of Applied Materials, SARChI Chair in Carbon Technology and Materials, University of Pretoria, Pretoria 0028, South Africa

[a)]**Author to whom correspondence should be addressed:** ncholu.manyala@up.ac.za. **Tel.:** + (27)12 420 3549. **Fax:** + (27)12 420 2516

ABSTRACT

In this work, a birnessite-type MnO_2/carbon composite with hierarchical nanostructures was synthesized using $KMnO_4$ solution and spent printing carbon grains. A hybrid electrochemical supercapacitor device was fabricated based on the birnessite-type MnO_2–carbon composite electrode and carbonized iron-polyaniline/nickel graphene foam as positive and negative electrodes, respectively. At the lowest specific current of 1.0 A g^{-1} and cell potential of 2.2 V in 2.5M KNO_3 electrolyte, the device displayed a high energy and power density of 34.6 W h kg^{-1} and 1100.0 W kg^{-1}, respectively. The device further displayed long-term cycling stability with a capacitance retention of 98% over 10 000 galvanostatic charge–discharge cycles at 10 A g^{-1}. This device displays the overall excellent electrochemical performance.

I. INTRODUCTION

Today, there is a great development of power systems due to the increased demand for highly reliable electricity and the consumption of renewable energy technologies. Power supply is a critical issue due to the rapid increase in electronic loads. Energy storage systems with vital power utility are in high demand. Among different types of energy storage systems, supercapacitors (SCs) have received great attention owing to their attractive properties, such as long life cycle stability, high power density, high efficiency, fast charge–discharge capability, and operational safety.[1–7] In general, SCs exhibit low energy densities, and this was the motivation for this study. To overcome low energy densities of SCs, one of the approaches is to develop new electrode materials for SCs (e.g., carbon materials, metal oxides/hydroxides/disulfides, and conducting polymers). The focus has also been on developing hybrid supercapacitors using battery-like electrode materials and pseudocapacitive electrodes since they display high capacity/capacitance.[8,9]

Conducting polymers for electrochemical energy storage applications have been studied extensively due to their high potential window, high conductivity, high storage capacity, and low cost.[10–13] The conducting polymers commonly used in SCs are polyaniline (PANI), polypyrrole (PPY), and polythiophene (PT).[14] The composites of these conducting polymers have shown enhanced electrochemical performance in SCs. Recent reports have shown that iron–polyaniline (Fe–PANI) composites attain high electrocatalytic and electrochemical performance with long-cycling stability.[7,15–17] Moreover, the PANI/graphene composite shows much better capacitance performance, and the synergy effect

between the two materials greatly improves the retention life of the composite material.[7,18,19] Among several metal oxides, birnessite-type manganese dioxide (MnO_2) has been studied extensively for SC application because it is low cost, naturally abundant, highly redox-active, and environmentally friendly, and it exhibits high pseudocapacitive performance in aqueous neutral electrolytes.[20–23] Despite the high electrochemical performance displayed by MnO_2 in aqueous neutral electrolytes, it has low electrical conductivity resulting in low cycling stability.[21,24] The low cycling stability of MnO_2 is improved by using carbon-based materials with excellent conductivity as a support during MnO_2 synthesis.[25–30]

Although studies about birnessite-type MnO_2-based materials as the positive electrode and activated carbon (AC) as the negative electrode have been extensively reported in the literature,[20–22,25,29–44] there are rare studies done on carbonized iron–polyaniline/nickel graphene foam (CFe/PANI/NiGF) as a negative electrode. In this work, we report on a hybrid electrochemical supercapacitor device based on the birnessite-type MnO_2C composite as the positive electrode and carbonized iron–polyaniline/nickel graphene foam as a negative electrode. The as-fabricated asymmetric device was performed at a cell potential of 0–2.2 V in 2.5M KNO_3. At a specific current of 1 A g^{-1}, this device displayed energy and power densities of 34.6 W h kg^{-1} and 1100.0 W kg^{-1}, respectively. Additionally, for both cycling and voltage holding tests, the device exhibited excellent stability.

II. EXPERIMENTAL

A. Synthesis of the as-prepared electrodes

MnO_2C with hierarchical nanostructures was synthesized using $KMnO_4$ solution and spent printing carbon grains [Scheme 1(a)]. In the synthesis, 0.6 g of spent printing carbon grains were dissolved in 32 ml of 2M $KMnO_4$ solution.[47] The mixture was then transferred into a sealed 50 ml Teflon-lined autoclave and kept at 160 °C for 18 h. The recovered product [MnO_2C composite with nanowires/microsponges morphology, Scheme 1(a)] was collected as a brown precipitant by several centrifugation and ethanol washing cycles. Briefly, the hydrothermal solid–liquid reaction is proposed as

$$4MnO_4^- + 3C \rightarrow 4MnO_2 + 2CO_3^{2-} + CO_2. \quad (1)$$

Fei *et al.*[47] referred to this hydrothermal method as a one-pot environmentally friendly process that changes toxic carbon grains from a spent inkjet cartridge into transition metal oxide hierarchical nanostructures through a limited hydrothermal redox reaction. Therefore, this does not only avoid the disposal of toxic carbon grains but also provides metal oxide nanostructures for energy storage applications.

The CFe/PANI/NiGF used as the negative electrode was prepared via a similar method to that reported in our previous work[7] [Scheme 1(b)]. Briefly, 0.4 g of PANI and 0.2 g of iron nitrate

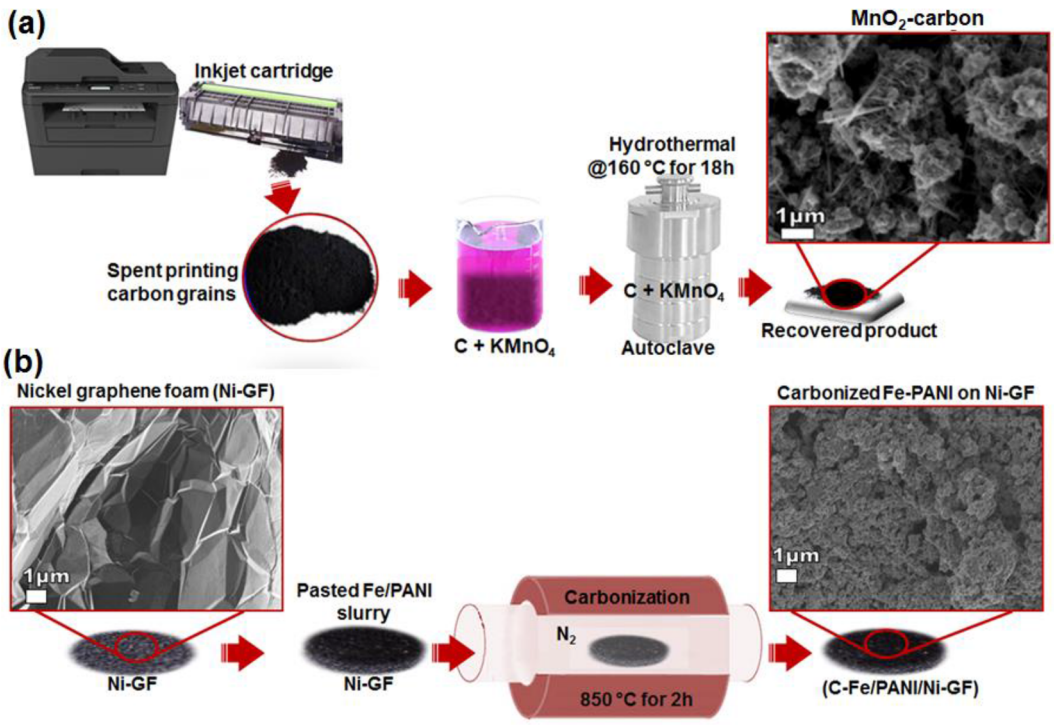

SCHEME 1. (a) The synthesis route for the MnO_2C composite using $KMnO_4$ solution and spent printing carbon grains. (b) The synthesis route for the carbonized Fe–PANI mixture on NiGF (CFe/PANI/NiGF).

nonahydrate [$Fe(NO_3)_3{\cdot}9H_2O$] were dissolved in 50 ml of ethanol and dispersed until the Fe–PANI slurry was formed. The slurry was pasted on graphene supported by nickel foam and carbonized at 850 °C (ramp rate of 10 °C min^{-1}) for 2 h under nitrogen gas. The difference between annealed NiGF (uncoated) and annealed material-coated NiGF gives the active material's substance load of the CFe/PANI/NiGF electrode.

B. Morphological, structural, compositional, and electrochemical characterization

The characterization of the as-prepared electrode materials was carried out using scanning electron microscopy (SEM, Zeiss Ultra Plus 55 field emission scanning electron microscope), energy-dispersive x-ray spectrometer (EDS), x-ray diffractometer (XRD), XPERTPRO diffractometer (PANalytical BV, Netherlands), Raman spectroscopy (WITec alpha300 RAS+ confocal Raman microscope with a 532 nm excitation laser and a laser power of 5 mW), and x-ray photoelectron spectroscopy (XPS) (Thermo Fisher photoelectron spectrometer fitted with a monochromatic Al Kα radiation x-ray source).

In the case of electrochemical characterization, a multi-channel Biologic VMP-300 potentiostat (Knoxville TN 37930, USA) was used in three- and two-electrode configurations. For three-electrode configuration, the MnO_2C composite electrode was obtained by coating a mixture of 80 wt. % MnO_2 (active material), 10 wt. % carbon black as a conductive additive, and 10 wt. % polyvinylidene fluoride (PVDF) binder dispersed in N-methylpyrrolidone (NMP) solution onto a nickel foam (1 × 1 cm^2). Thereafter, the electrode was dried at 60 °C overnight. The masses of the active materials of the MnO_2C composite and CFe/PANI/NiGF were 3.8 mg/cm^2 and 1.9 mg/cm^2, respectively. The CFe/PANI/NiGF working electrode was prepared as discussed in Scheme 1(b). The measurements were carried out in 2.5M KNO_3 electrolyte using a glassy carbon plate as the counter electrode, Ag/AgCl (saturated with 3M KCl) reference electrode, and MnO_2C composite and CFe/PANI/NiGF served as positive and negative working electrodes, respectively. For two-electrode configuration, masses of positive and negative working electrodes were 1.7 mg/cm^2 and 2.5 mg/cm^2, respectively. The asymmetric device was fabricated using 2.5M KNO_3 aqueous electrolyte. The specific capacitance (C_S) was calculated for both three-electrode and two-electrode configurations using Eq. (1),[7,48–50]

$$C_s = \frac{I\Delta t}{m\Delta V}, \tag{2}$$

where I/m is the specific current (A/g), m is the mass of the electrode material (g), Δt is the discharge time (s), and ΔV is the maximum potential. The mass balance between the two electrodes is expressed as[51]

$$\frac{m_+}{m_-} = \frac{C_{s(-)} \times \Delta V_-}{C_{s(+)} \times \Delta V_+}, \tag{3}$$

where $C_{S(+)}$, $C_{S(-)}$, m_+, m_-, ΔV_+, and ΔV_- are the specific capacitances, masses, and maximum potential windows of the active materials in positive and negative electrodes, respectively. The energy density E_d and the power density P_d of the device were calculated using the following equations:

$$E_d\left(\text{W h kg}^{-1}\right) = \frac{C_s\Delta V^2}{7.2}, \tag{4}$$

$$P_d\left(\text{W kg}^{-1}\right) = \frac{3600E_d}{\Delta t}, \tag{5}$$

where C_S is the specific capacitance, ΔV is the maximum cell potential, and Δt is the discharge time (s).

III. RESULTS AND DISCUSSION

A. Morphological, structural, and compositional characterization

The morphologies of the as-prepared materials were examined using SEM, as shown in Fig. 1. Figures 1(a) and (1(b) display the morphology of the MnO_2C composite at low and high magnifications, respectively. In these figures, the MnO_2C composite shows a combined morphology of nanowires and microsponges (sponge-like hierarchical nanostructures). Fei *et al.* have observed a similar morphology for MnO_2 prepared using the same synthesis method and conditions.[47] Figure 1(c) shows the morphology of NiGF, which shows graphene wrinkles and ripples on the Ni template.[52] The carbonized iron–polyaniline on nickel graphene foam (CFe/PANI/NiGF) shows a different morphology from NiGF, i.e., agglomerated nanograins [Figs. 1(d) and 1(e)].

The elemental composition of the as-prepared materials, MnO_2C composite, and CFe/PANI/NiGF was obtained using EDS, and the results are shown in Fig. 2. Figure 2(a) shows the average EDS spectrum of the MnO_2C composite, which displays the main elements Mn, O, and K, and a significant amount of C. In Fig. 2(a), the presence of K is from the synthesis, i.e., $KMnO_4$ solution. Figure 2(b) displays the average EDS spectrum of CFe/PANI/NiGF, which shows the main elements Fe, S, O, N, C, and Ni. The detected Ni is from the Ni template from which graphene was grown, and S is attributed to the PANI precursor (ammonium persulfate), which degraded during pyrolysis.[17]

Figure 3(a) shows the XRD pattern of the as-prepared MnO_2C composite, which displays the characteristic diffraction peaks of the birnessite-type MnO_2C composite with peaks corresponding to (121) and (002) planes. The matching Inorganic Crystal Structure Database (ICSD) Card No. 20227 was used to index the diffraction peaks. The diffraction peak at around 26° is associated with the (002) plane of graphitic carbon. Figure 3(b) shows the XRD pattern of the as-prepared carbonized iron–PANI (CFe/PANI) without NiGF, which matches the diffraction peak positions of the orthorhombic Fe_3C (ICSD No. 16593) and FeS (ICSD No. 35008). In addition, the diffraction peaks matching Fe (ICSD No. 64795) are also observed, which suggest that during the pyrolysis process, the Fe cations were reduced to metallic Fe.[53]

Furthermore, the Raman spectrum of the as-prepared MnO_2C composite [Fig. 3(c)] shows a broad peak at 640 cm^{-1} with a shoulder at 495 cm^{-1} and 570 cm^{-1}, which agree with the main vibrational features of the birnessite-type MnO_2.[54] The presence of carbon traces in the as-prepared MnO_2C composite is shown by the D (~1346 cm) and G (1587 cm^{-1}) peaks, which are characteristic of the disordered carbon and the tangential vibrations of the

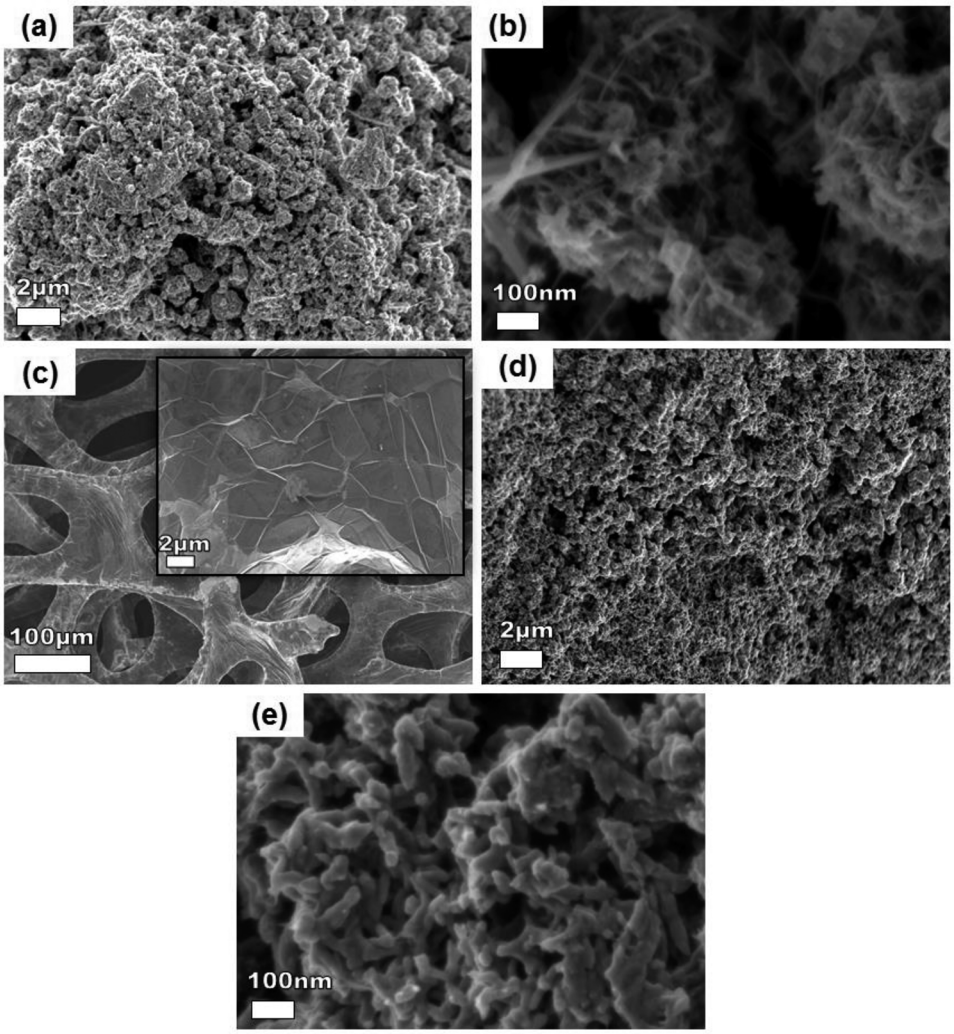

FIG. 1. SEM images: [(a) and (b)] low and high magnification images of the MnO_2C composite, respectively. (c) Low and high magnification images of NiGF (inset of the figure). [(d) and (e)] Low and high magnification images of CFe/PANI/NiGF, respectively.

sp^2-hybridized carbon, respectively.[55] Figure 3(d) shows the Raman spectrum of the as-prepared CFe/PANI/NiGF. From this figure, the D and G bands in the range of 1240–1700 cm^{-1} are observed, and these are attributed to the functional groups of PANI (i.e., CN at ~1210 cm^{-1} and 1346 cm^{-1}, CC at 1412 cm^{-1}, C=N at 1490 cm^{-1}, C=C at 1585 cm^{-1} and CC at 1610 cm^{-1}).[56,57] Additionally, the observed Fe–PANI vibration bands in the range of 100–700 cm^{-1} [Fig. 3(e)] are attributed to orthorhombic sulfur α-S_8 (153 cm^{-1}, 223 cm^{-1}, and 471 cm^{-1}),[58,59] FeS (191 cm^{-1}, 205 cm^{-1}, 265 cm^{-1}, and 290 cm^{-1}),[59,60] α-FeOOH (310 cm^{-1}), γ-FeOOH (360 cm^{-1} and 540 cm^{-1}),[59,61] Fe_3C (223 cm^{-1}, 290 cm^{-1}, 360 cm^{-1}, and 603 cm^{-1}),[62] and γ-Fe_2O_3/Fe_3O_4 (680 cm^{-1}).[61,63] It is worth noting that the phases observed in the Fe–PANI range [Fig. 3(e)] have x-ray diffraction peaks (α-S_8 ICSD No. 27261, α-FeOOH ICSD No. 77327, γ-FeOOH ICSD No. 93948, Fe_2O_3 ICSD No. 64599, and Fe_3O_4 ICSD No. 35000), which overlap with the diffraction peaks of the phases shown in the XRD pattern of the CFe/PANI/NiGF [Fig. 3(b)].[7] In Fig. 3(d), the characteristic Raman signature of graphene foam is not observed, and this is because the graphene is coated by Fe/PANI, as can be seen from the SEM images. Nonetheless, the interaction between the Fe/PANI and graphene foam during pyrolysis is energetically favorable owing to the unpaired π-electron in graphene and the high electronegativity of oxygen and sulfur present in the material.[7] Figure 3(f) shows the characteristic Raman spectra of as-prepared NiGF, which displays the main features of the Raman spectrum of graphene. These spectra are a characteristic Raman spectrum of a monolayer (top), bilayer (middle), and few-layer (bottom) graphene with 2D-to-G peak intensity ratios of >2, ~1, and <0.6, respectively.[7,64] Figure 3(f) reveals the layers of NiGF as discussed in our recent work.[7]

Figure 4(a) shows the core level spectra of C 1s, K 2p, Mn 2p, and O 1s obtained from the as-prepared MnO_2C composite. The core level spectrum of C 1s of the MnO_2C composite material shows a peak at 284.6 eV attributed to the C=C and C−C bonds,

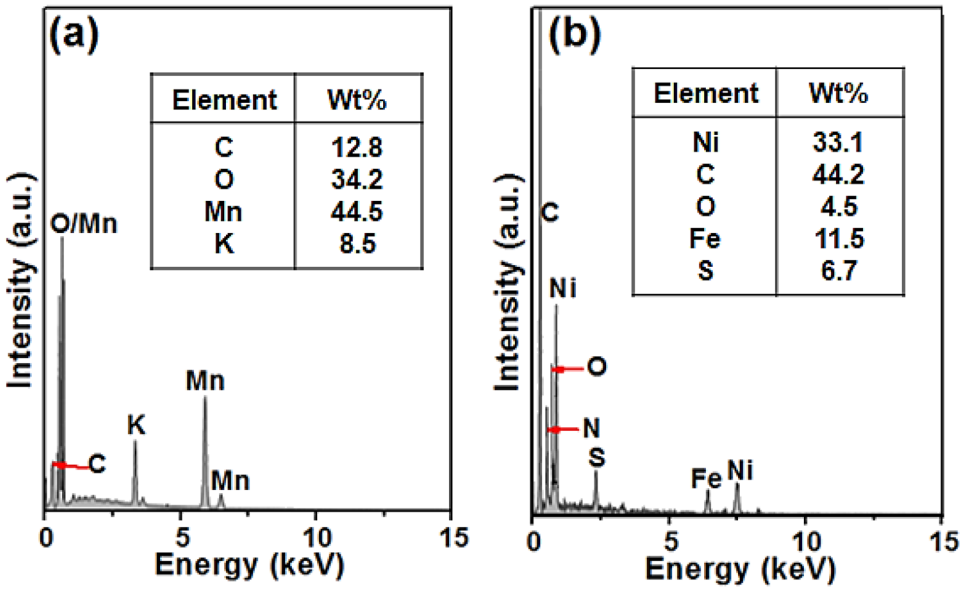

FIG. 2. Average EDS spectra: (a) MnO_2C composite and (b) CFe/PANI/NiGF.

and the broadness of the peak is due to the carbon-oxide components present in the sample. The core level spectrum of K 2p confirms the presence of potassium oxide in the material, which arises from $KMnO_4$ used in the synthesis of the MnO_2C composite. The core level spectrum of Mn 2p shows Mn $2p_{3/2}$ and Mn $2p_{1/2}$ peaks at the binding energy of 642.8 eV and 654.2 eV, respectively. The core level spectrum of O 1s shows a strong peak at 529.8 eV with a shoulder from ~530.9 eV to 534 eV, which could be predominantly due to MnO bonds. Furthermore, Fig. 4(b) shows the core level spectra of C 1s, S 2p, Fe 2p, N 1s, and O 1s obtained from the as-prepared CFe/PANI/NiGF. From these XPS core level spectra, the C 1s peak at 284.6 eV appears broad and asymmetric due to different carbon compounds/oxides (e.g., COH/CN at 286.5 eV, COC at 287.6 eV, C=O at 288.9 eV, etc.) present in the sample, which are attributed to the functional groups of PANI.[65,66] The core level spectrum of S 2p shows peaks at 160.7 eV and 161.9 eV corresponding to S $2p_{3/2}$ and S $2p_{1/2}$ levels, respectively. These peaks are attributed to the S^{2-} ions and also confirm the FeS, SC, SS, and SS/SC bond-related peaks, which appear at 161.9 eV, 163.2 eV, 163.8 eV, and 164.8 eV, respectively.[67] The Fe 2p spectrum shows one of the binding energy peaks at 706.8 eV, which corresponds to Fe^0, Fe^{2+}, and Fe^{3+} ions.[68] The N 1s spectrum shows nitrogencarbon bond-related peaks at 398.7 eV (pyridinic N), 400.4 eV (pyrrolic N), and 401.5 eV (graphitic N).[69] The spectrum of O 1s shows a broad and asymmetric peak at 532.3 eV due to oxygen components, such as COH/COC and C=O, which appears at 532.7 eV and 530.9 eV, respectively.[70]

B. Electrochemistry

The as-prepared electrodes were evaluated in three-electrode and two-electrode systems using 2.5M KNO_3 electrolyte. In three-electrode configuration, the CV curves of the as-prepared positive (MnO_2C composite) and negative (CFe/PANI/NiGF) electrodes at different scan rates (5–100 mV s^{-1}) in the potential window range of 0.0–1.1 V vs Ag/AgCl and −1.1 V to 0.0 V vs Ag/AgCl are presented in Figs. 5(a) and 5(b), respectively. Figure 5(a) shows the CV curves of the positive electrode, which show symmetric quasi-rectangular and reversible pseudocapacitive behavior. Similarly, the CV curves of the negative electrode displayed in Fig. 5(b) show pseudocapacitive behavior without obvious redox peaks.[7] The CV curves are in agreement with the GCD curves of positive and negative electrodes, which are presented in Figs. 5(c) and 5(d), respectively. The GCD curves of the as-prepared electrodes also show pseudocapacitive behavior. Due to this behavior, the specific capacitance of the as-prepared electrodes was calculated from GCD curves using Eq. (2). The plot of specific capacitance as a function of a specific current is shown in Fig. 5(e). The specific capacitances of the as-prepared electrodes (positive and negative) are 76.8 F g^{-1} and 114.4 F g^{-1} at a specific current of 2 A g^{-1}, respectively.

The as-prepared electrodes were further tested in two-electrode configuration; the electrochemical performance of the as-prepared electrodes was fully explored by fabricating an asymmetric device as shown in Fig. 6(a). The charge balance ($Q_+ = Q_-$) of the two electrodes is required since they have different specific capacitances [Fig. 5(e)], where $Q_+ = C_{S(+)} \times m_+ \times \Delta V_+$ and $Q_- = C_{S(-)} \times m_- \times \Delta V_-$ are charges stored in both positive and negative electrodes, respectively. The mass balance was expressed using Eq. (3). From Fig. 5(e), the mass ratio ($m_+/m_- \approx 0.7$) at a specific current of 2 A g^{-1} was used for mass balance. Consequently, the masses of the positive electrode and negative electrode were obtained as 1.7 mg/cm^2 and 2.5 mg/cm^2, respectively, which gives the total mass of the cell as 4.2 mg/cm^2.

The as-fabricated MnO_2C//CFe/PANI/NiGF asymmetric device was able to reach the potential of 2.2 V [Fig. 6(b)]. The CV curves of the device [Fig. 6(c)] show pseudocapacitive behavior; with the increase in scan rate, the CV curves do not change, hence suggesting

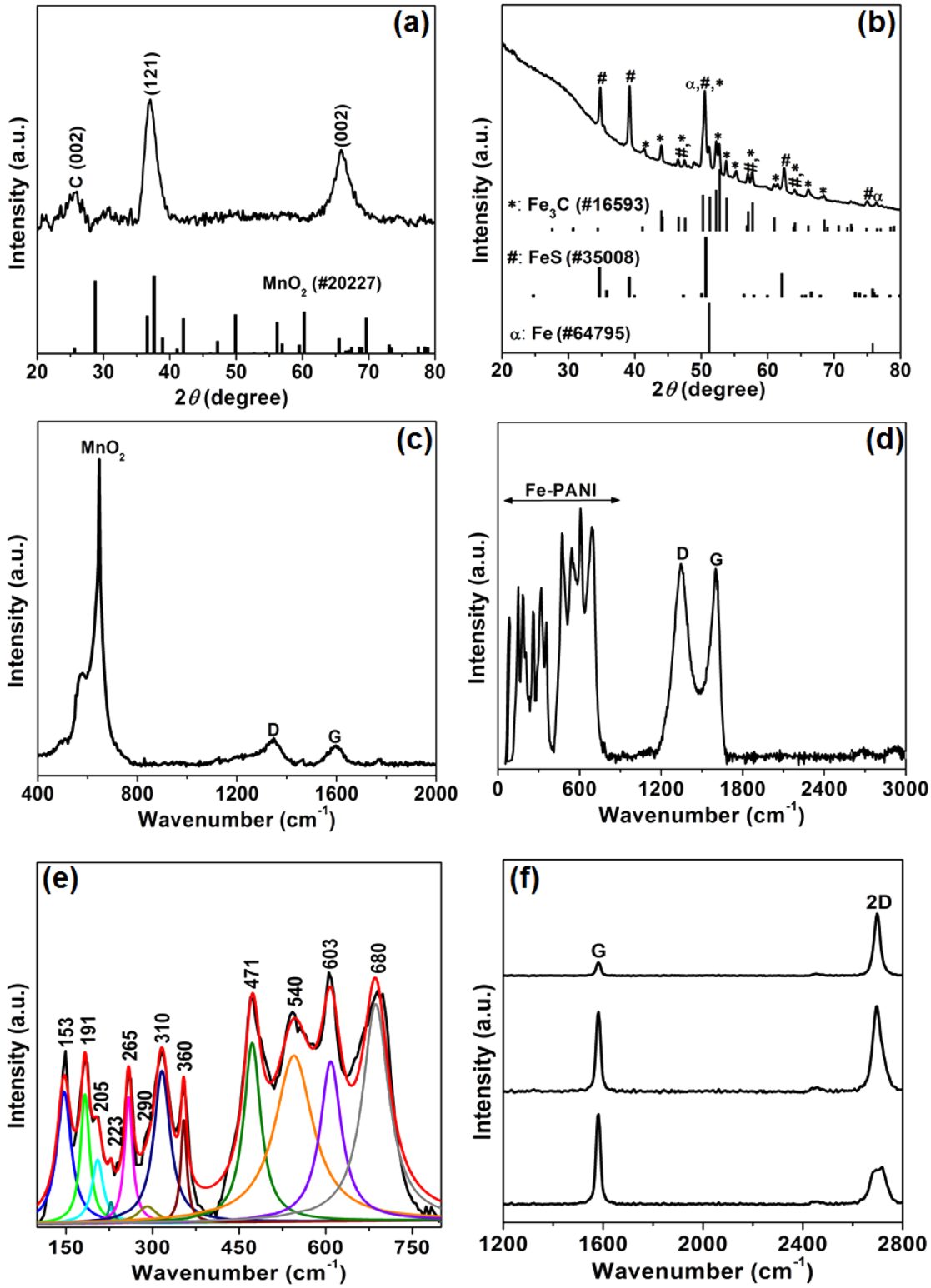

FIG. 3. [(a) and (b)] The XRD pattern and the matching ICSD cards of the as-prepared electrodes, MnO_2C composite, and CFe/PANI/NiGF, respectively. Raman spectra of (c) MnO_2C composites, [(d) and (e)] CFe/PANI/NiGF, and (f) NGF.

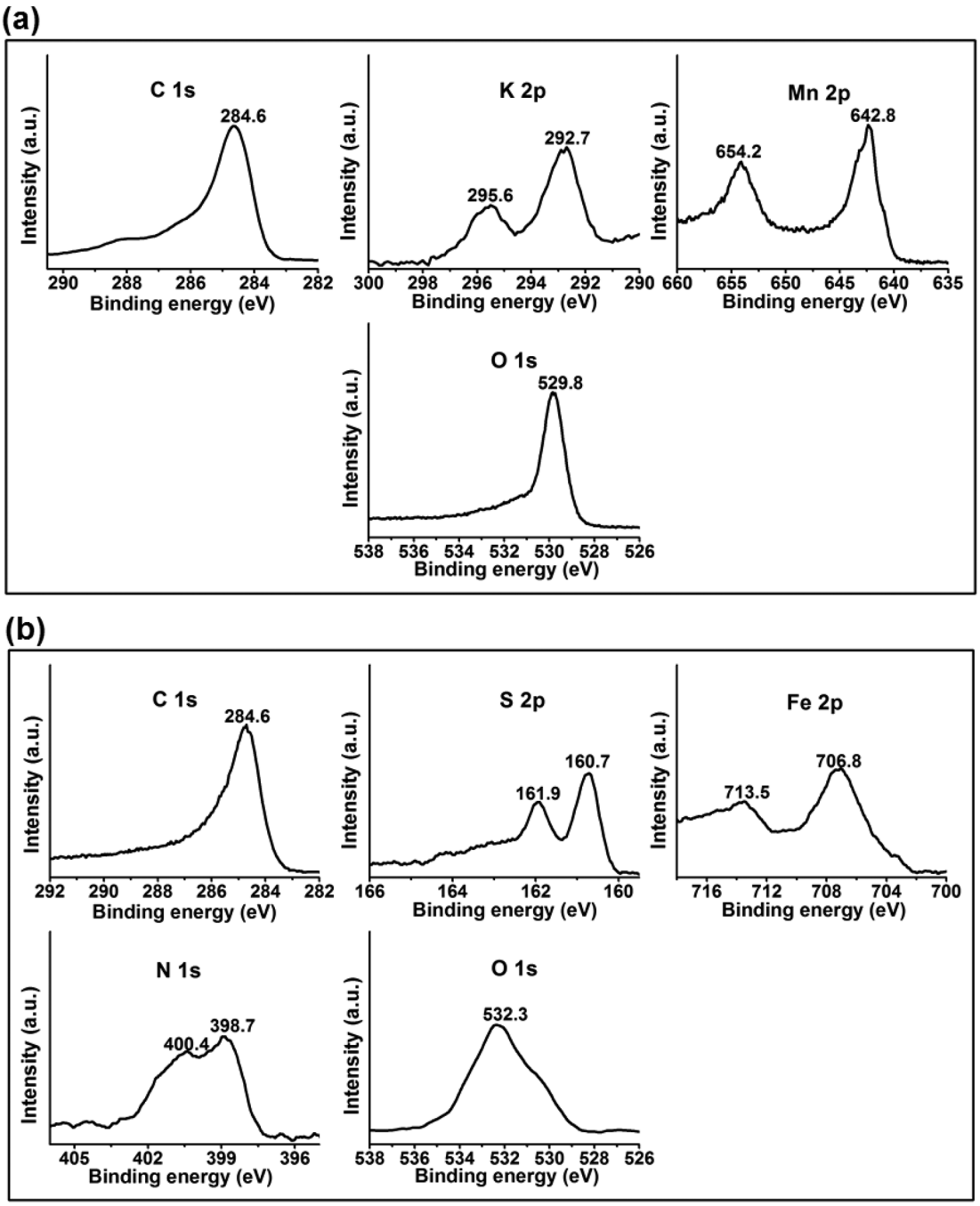

FIG. 4. The XPS core level spectra obtained from the as-prepared (a) MnO_2 and (b) CFe/PANI/NiGF.

that the device is stable. The GCD curves of the device at different specific currents in the range of 1 A g^{-1}–10 A g^{-1} are shown in Fig. 6(d). The specific capacitance of the device as a function of the specific current is shown in Fig. 6(e). At a low specific current of 1 A g^{-1}, the device exhibited a high specific capacitance of 51.5 F g^{-1}, and this is maintained at 30.6 F g^{-1} at a high specific current of 10 A g^{-1}.

The energy density (E_d) and the power density (P_d) of the device were calculated from the GCD curves using Eqs. (4) and (5), respectively. The Ragone plot in Fig. 7(a) shows the energy density

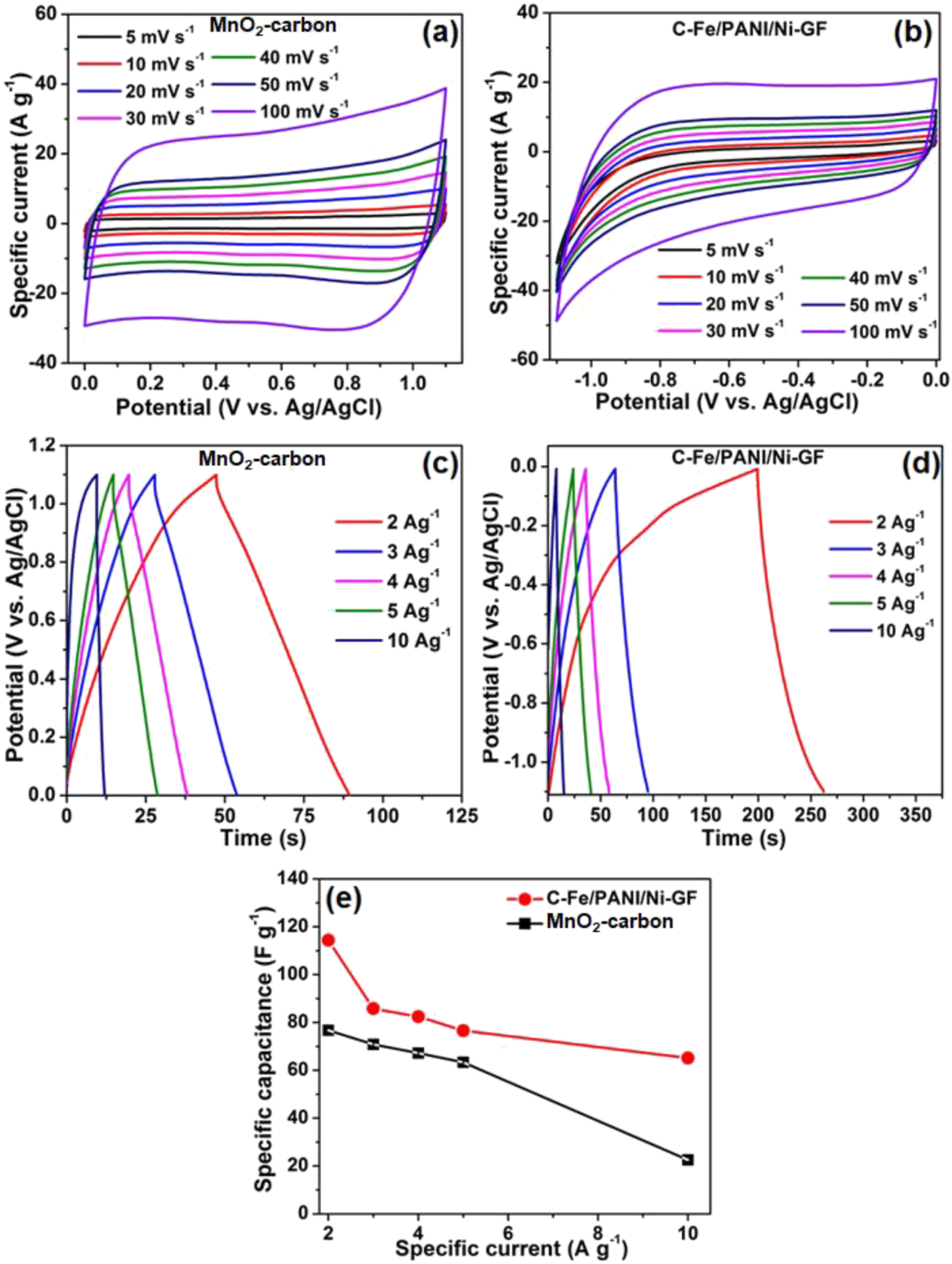

FIG. 5. [(a) and (b)] CV curves of positive and negative electrodes at different scan rates in the potential window range of 0.0–1.1 V and −1.1 V to 0.0 V, respectively. [(c) and (d)] GCD curves of the positive and negative electrodes at different specific currents in the range of 2 A g^{-1}–10 A g^{-1}, respectively. (e) The specific capacitance of both electrodes as a function of specific current.

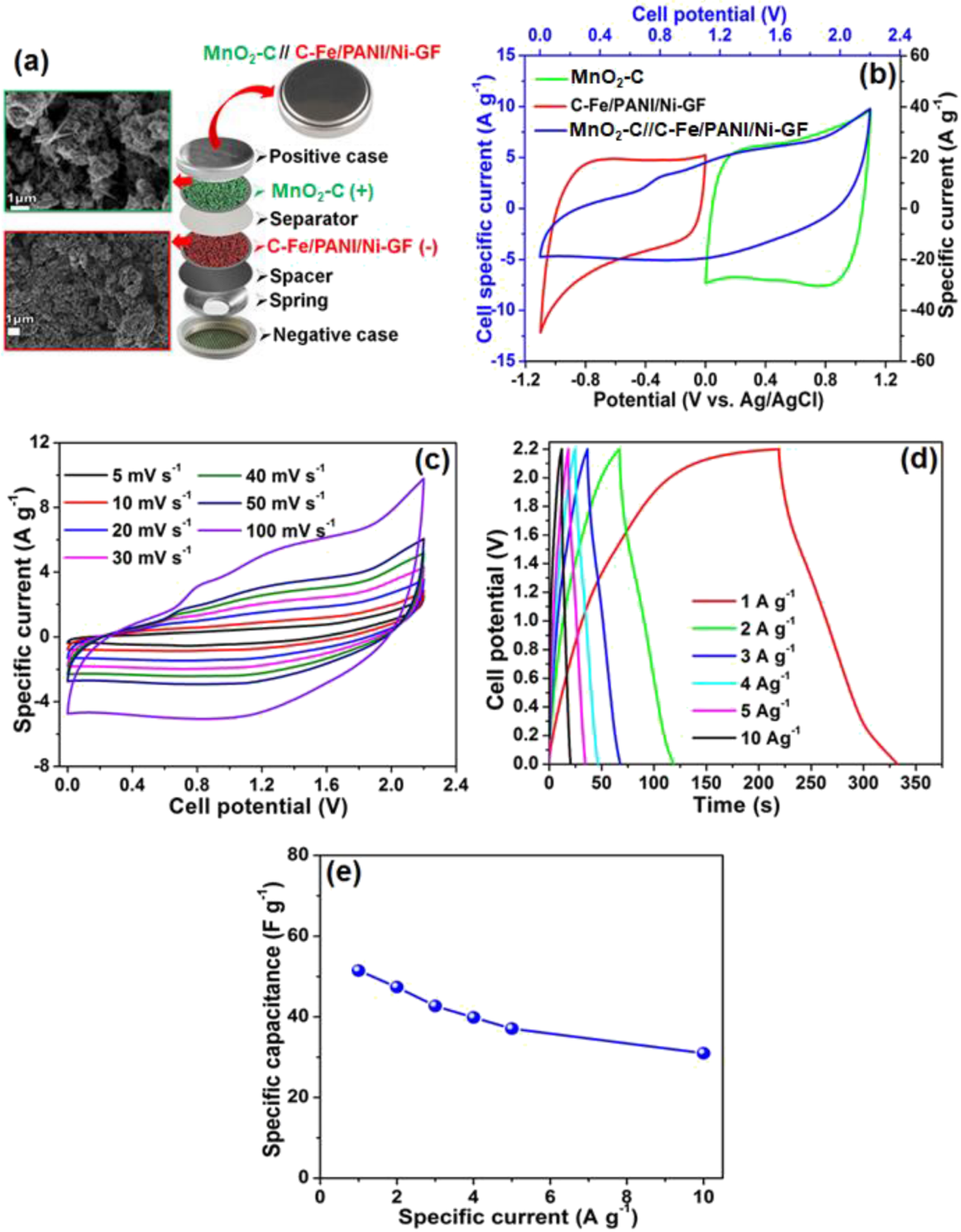

FIG. 6. (a) Scheme of the as-fabricated asymmetric supercapacitor device based on the MnO_2C composite as a positive and CFe/PANI/NiGF as a negative. (b) CV curves of both positive and negative electrodes at a scan rate of 100 mV s^{-1} evaluated in three-electrode and the as-fabricated MnO_2C//CFe/PANI/NiGF asymmetric device. For the as-fabricated asymmetric device: (c) CV curves at different scan rates in the range of 5–100 mV s^{-1}, (d) GCD curves at different current densities in the range of 1–10 A g^{-1}, and (e) the specific capacitance as a function of the specific current.

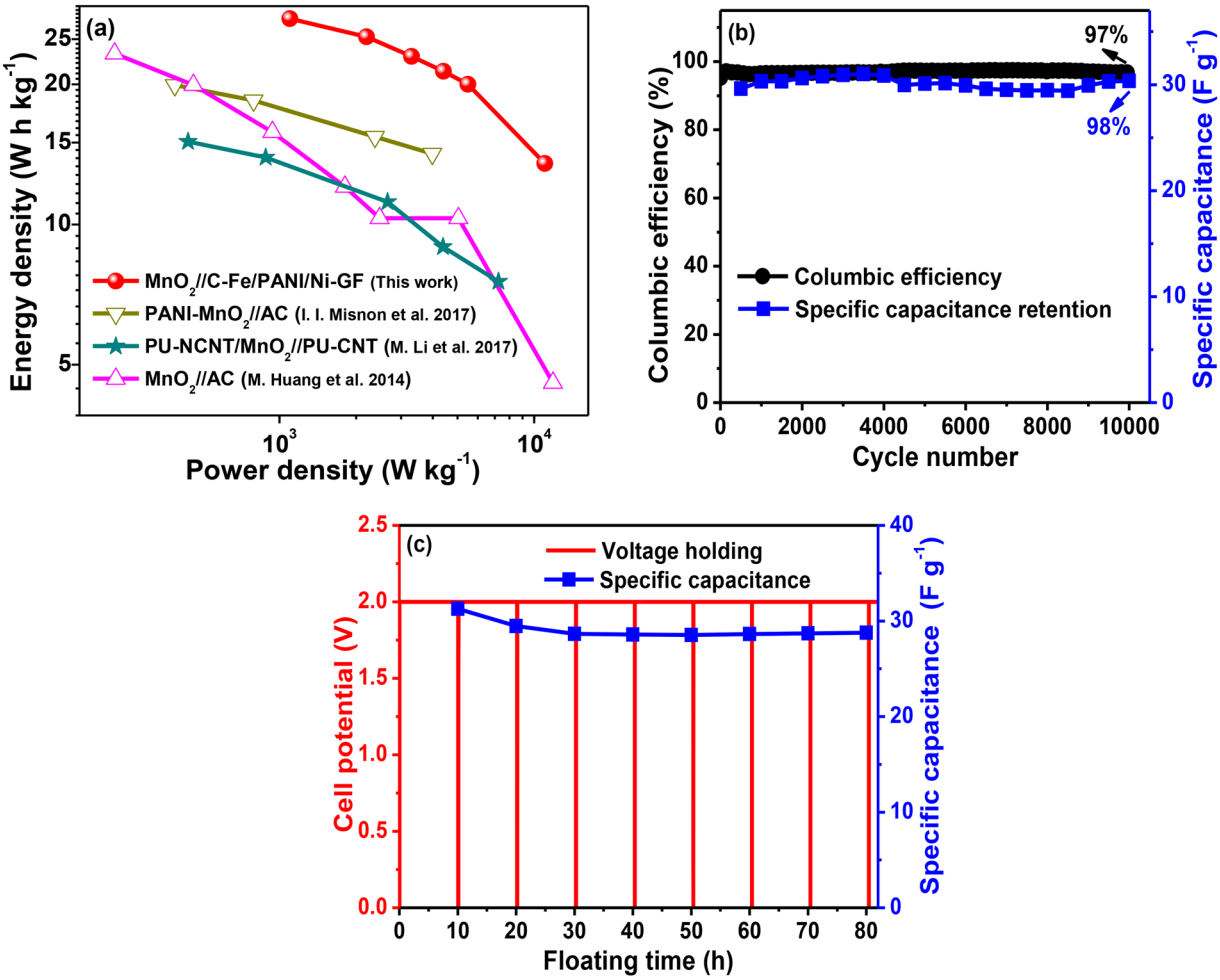

FIG. 7. (a) Energy and power densities of the MnO_2C//CFe/PANI/NiGF asymmetric device and MnO_2-based asymmetric devices reported in the literature. (b) The cycling stability test for the as-fabricated device at a specific current of 10 A g^{-1}. (c) Voltage holding and specific capacitance as a function of floating time evaluated at a specific current of 10 A g^{-1}.

as a function of power density. The as-fabricated asymmetric device exhibited a maximum energy density of 34.6 W h kg^{-1} and the corresponding power density of 1100.0 W kg^{-1}, at a specific current of 1.0 A g^{-1}. At a high specific current of 10 A g^{-1}, the device exhibited a high energy density of 20.6 W h kg^{-1} and the corresponding maximum power density of 11 661.7 W kg^{-1}. The as-fabricated asymmetric device exhibited energy and power densities that are higher than or comparable to MnO_2-based asymmetric devices reported in the literature as shown in Fig. 7(a) and Table I. These values of energy and power densities are quite impressive especially that at such high energy density values, the power density values are this high, which is not usually the case. Figure 7(b) shows the cycling stability test of the as-fabricated asymmetric device performed at a specific current of 10 A g^{-1}. The device exhibited a columbic efficiency of 97% and 98% capacitance retention after a 10 000th galvanostatic charge–discharge cycle. The stability of the device was further tested using voltage holding at 10 A g^{-1} and a maximum operating potential of 2.2 V for 80 h, as shown in Fig. 7(c). The figure shows excellent stability in the specific capacitance of the device over 80 h of voltage holding.

The electrochemical impedance spectroscopy analysis of the as-fabricated asymmetric device before and after cycling stability was carried out, as shown by the Nyquist plot in Fig. 8(a). The Nyquist plot shows a linear component in the low-frequency region, which is slightly tilted with bigger angle than 45° signifying a deviation from ideal capacitive behavior. An ideal supercapacitor exhibits a typical vertical line parallel to the y axis with a mass capacitance (Q_2). The intersection of the Nyquist plot on the x axis in the high-frequency region describes the equivalent series resistance (R_S), which is in series with the charge transfer resistance (R_{CT}) and Warburg impedance characteristic element (W) connected in parallel to the real capacitance (Q_1) [see the inset of Fig. 8(b)].[71]

TABLE I. Electrochemical performance comparison of MnO_x-based aqueous electrochemical capacitors.

Positive electrode	Negative electrode	Electrolyte	Current density (A g^{-1})	Potential window (V)	Energy density (W h kg^{-1})	Power density (W kg^{-1})	References
MnO_2	AC	1M Na_2SO_4	0.1	2.0	17.1	100	Zhang *et al.*[41]
MnO_2	AC	1M Na_2SO_4	0.25	1.8	22.5	146 200	Huang *et al.*[20]
MnO_2	AC	0.1M K_2SO_4	0.55	2.2	17.3	605	Cottineau *et al.*[42]
MnO_2	AC	0.5M K_2SO_4	...	1.8	28.4	150	Qu *et al.*[43]
OLC/Mn_3O_4	AC	1M Na_2SO_4	0.1	2.0	19.0	45 000[a]	Makgopa *et al.*[44]
PANI–MnO_2	AC	6M KOH	0.5	1.6	20	400	Misnon and Jose[45]
MnO_2/CNT	AC	1M Na_2SO_4	0.25	1.8	27.0	225	Gueon and Moon[25]
MnO_2/CNT	AC	0.5M Na_2SO_4	1.0	2.0	13.9	...	Demarconnay *et al.*[22]
MnO_2/CNT	AC	2M KNO_3	0.1	2.0	21.0	123	Khomenko *et al.*[46]
Graphene/MnO_2	AC	1M Na_2SO_4	...	1.8	51.1[b]	102.2[b]	Fan *et al.*[31]
MnO_2/CNT	AC	1M Na_2SO_4	1.0	1.5	13.3	600	Li *et al.*[21]
MnO_2–CNT	AC	1M Li_2SO_4	0.5	2.0	24.58	500	Ochai-Ejeh *et al.*[32]
MnO_2graphene	Graphene	1M Na_2SO_4	2.23	1.7	10.03	2 530	Deng *et al.*[33]
Graphene/MnO_2	Graphene	1M Na_2SO_4	5.0	2.0	7.0	5 000	Wu *et al.*[34]
MnO_2	Graphene	0.5M Na_2SO_4	1.0	2.0	23.2	1 000	Gao *et al.*[35]
Graphene/MnO_2	Graphene/Ag	1M Na_2SO_4	...	1.8	50.8[b]	101[b]	Shao *et al.*[36]
MnO_2	CNTs	1M Na_2SO_4	0.2	2.0	47.4	200	Jiang *et al.*[37]
MnO_2	Bacterial cellulose	1M Na_2SO_4	1.0	2.0	32.91	284 630	Chen *et al.*[38]
PU–NCNT/MnO_2	PU–CNT	1M Na_2SO_4	1.0	1.8	14.76	~438	Li *et al.*[39]
OLC/MnO_2	OLC/MnO_2	1M Na_2SO_4	0.1	0.8	5.6	74 800[a]	Makgopa *et al.*[40]
MnO_2	Fe_3O_4	0.1M K_2SO_4	0.45	1.8	8.1	405	Cottineau *et al.*[42]
MnO_2C	CFe/PANI/NiGF	2.5M KNO_3	1.0	2.2	34.6	1 100	This work

[a]Calculation based on the EIS maximum power (P_{max}).
[b]Calculation from CV curves.

The Nyquist plot of the device before and after cycling stability shows a comparable R_S of ~1 Ω [see the inset of Fig. 8(a)] indicating that the electrodes have good chemical stability. The circuit diagram was used to fit the Nyquist plot [inset of Fig. 8(b)]. The circuit diagram indicates that the deviation of the supercapacitor behavior from an ideal capacitive behavior is attributed to a leakage resistance (R_L), which is parallel to the mass capacitance (Q_2).[72,73]

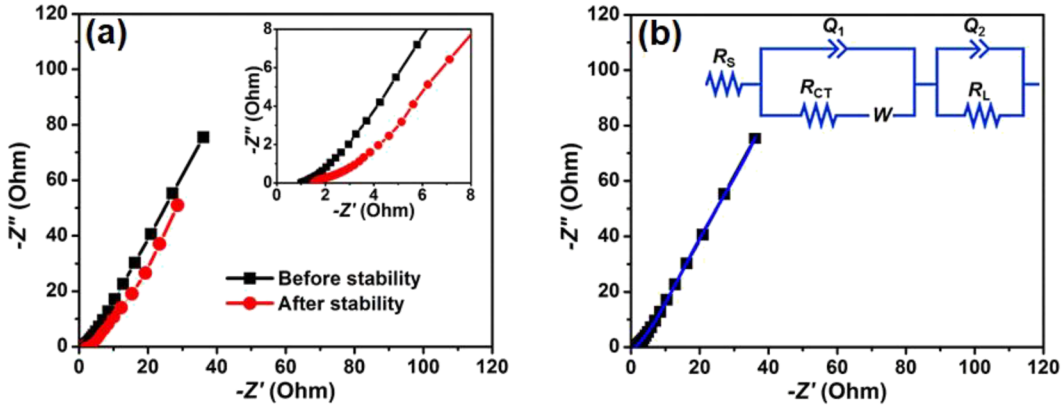

FIG. 8. (a) Nyquist plots of the as-fabricated asymmetric device before and after stability (the inset shows the enlarged high-frequency region). (b) The Nyquist plot and the fit of the equivalent circuit diagram in the inset of the figure.

IV. CONCLUSION

In this work, the CFe/PANI was grown on NiGF and showed improvement in electrochemical properties. The asymmetric device was fabricated based on the birnessite-type MnO_2carbon composite and the CFe/PANI/NiGF as positive and negative electrodes, respectively. The as-fabricated asymmetric device at a specific current of 1.0 A g^{-1} and cell potential window of 0.0–2.2 V exhibited maximum energy and power densities of 34.6 W h kg^{-1} and 1100.0 W kg^{-1}, respectively. At a high specific current of 10 A g^{-1}, the device exhibited a high energy density of 20.6 W h kg^{-1} and a corresponding maximum power density of 11 661.7 W kg^{-1}. The device displayed remarkable stability with a capacitance retention of 98% up to 10 000 constant GCD cycles. The stability was tested further using voltage holding at a potential of 2.2 V up to 80 h and still displayed excellent stability.

ACKNOWLEDGMENTS

This work was based on research supported by the South African Research Chairs Initiative (SARChI) of the Department of Science and Technology and the National Research Foundation (NRF) of South Africa (Grant No. 61056). Any opinion, finding and conclusion, or recommendation expressed in this material is that of the authors, and the NRF does not accept any liability in this regard. M. N. Rantho acknowledges the funding from the University of Pretoria and NRF through SARChI in Carbon Technology and Materials.

DATA AVAILABILITY

The data that support the findings of this study are available from the corresponding author upon reasonable request.

REFERENCES

[1] S. W. Zhang and G. Z. Chen, "Manganese oxide based materials for supercapacitors," Energy Mater. **3**, 186–200 (2008).
[2] E. Frackowiak and F. Béguin, "Carbon materials for the electrochemical storage of energy in capacitors," Carbon **39**, 937–950 (2001).
[3] H. Pan, J. Li, and Y. P. Feng, "Carbon nanotubes for supercapacitor," Nanoscale Res. Lett. **5**, 654–668 (2010).
[4] L. L. Zhang and X. S. Zhao, "Carbon-based materials as supercapacitor electrodes," Chem. Soc. Rev. **38**, 2520 (2009).
[5] E. Frackowiak, "Carbon materials for supercapacitor application," Phys. Chem. Chem. Phys. **9**, 1774 (2007).
[6] S. Mondal, U. Rana, and S. Malik, "Reduced graphene oxide/Fe_3O_4/polyaniline nanostructures as electrode materials for an all-solid-state hybrid supercapacitor," J. Phys. Chem. C **121**, 7573–7583 (2017).
[7] M. N. Rantho, M. J. Madito, and N. Manyala, "High-performance symmetric supercapacitor device based on carbonized iron-polyaniline/nickel graphene foam," J. Alloys Compd. **819**, 152993 (2019).
[8] W. Zuo, R. Li, C. Zhou, Y. Li, J. Xia, and J. Liu, "Battery-supercapacitor hybrid devices: Recent progress and future prospects," Adv. Sci. **4**, 1–21 (2017).
[9] F. Wang, X. Wu, X. Yuan, and Z. Liu, "Latest advances in supercapacitors: From new electrode materials to novel device designs," Chem. Soc. Rev. **46**, 6816–6854 (2017).
[10] G. Wang, L. Zhang, and J. Zhang, "A review of electrode materials for electrochemical supercapacitors," Chem. Soc. Rev. **41**, 797–828 (2012).
[11] K. R. Prasad, K. Koga, and N. Miura, "Electrochemical deposition of nanostructured indium oxide: High-performance electrode material for redox supercapacitors," Chem. Mater. **16**(10), 1845–1847 (2004).
[12] M. Kalaji, P. J. Murphy, and G. O. Williams, "The study of conducting polymers for use as redox supercapacitors," Synth. Met. **102**, 1360–1361 (1999).
[13] Y. Zhou, B. He, W. Zhou, J. Huang, X. Li, B. Wu, and H. Li, "Electrochemical capacitance of well-coated single-walled carbon nanotube with polyaniline composites," Electrochim. Acta **49**, 257–262 (2004).
[14] K. S. Ryu, K. M. Kim, N.-G. Park, Y. J. Park, and S. H. Chang, "Symmetric redox supercapacitor with conducting polyaniline electrodes," J. Power Sources **103**, 305–309 (2002).
[15] H. Mi, X. Zhang, X. Ye, and S. Yang, "Preparation and enhanced capacitance of core–shell polypyrrole/polyaniline composite electrode for supercapacitors," J. Power Sources **176**, 403–409 (2008).
[16] C. Portet, P. L. Taberna, P. Simon, E. Flahaut, and C. Laberty-Robert, "High power density electrodes for carbon supercapacitor applications," Electrochim. Acta **50**, 4174–4181 (2005).
[17] M. N. Rantho, M. J. Madito, and N. Manyala, "Symmetric supercapacitor with supercapattery behavior based on carbonized iron cations adsorbed onto polyaniline," Electrochim. Acta **262**, 82 (2018).
[18] H. Wang, Q. Hao, X. Yang, L. Lu, and X. Wang, "A nanostructured graphene/polyaniline hybrid material for supercapacitors," Nanoscale **2**, 2164 (2010).
[19] M. Yu, Y. Huang, C. Li, Y. Zeng, W. Wang, Y. Li, P. Fang, X. Lu, and Y. Tong, "Building three-dimensional graphene frameworks for energy storage and catalysis," Adv. Funct. Mater. **25**, 324–330 (2015).
[20] M. Huang, Y. Zhang, F. Li, L. Zhang, R. S. Ruoff, Z. Wen, and Q. Liu, "Self-assembly of mesoporous nanotubes assembled from interwoven ultrathin birnessite-type MnO_2 nanosheets for asymmetric supercapacitors," Sci. Rep. **4**, 3878 (2014).
[21] L. Li, Z. A. Hu, N. An, Y. Y. Yang, Z. M. Li, and H. Y. Wu, "Facile synthesis of MnO_2/CNTs composite for supercapacitor electrodes with long cycle stability," J. Phys. Chem. C **118**, 22865–22872 (2014).
[22] L. Demarconnay, E. Raymundo-Piñero, and F. Béguin, "Adjustment of electrodes potential window in an asymmetric carbon/MnO_2 supercapacitor," J. Power Sources **196**, 580–586 (2011).
[23] T. Brousse, P.-L. Taberna, O. Crosnier, R. Dugas, P. Guillemet, Y. Scudeller, Y. Zhou, F. Favier, D. Bélanger, and P. Simon, "Long-term cycling behavior of asymmetric activated carbon/MnO_2 aqueous electrochemical supercapacitor," J. Power Sources **173**, 633–641 (2007).
[24] Y. Jin, H. Chen, M. Chen, N. Liu, and Q. Li, "Graphene-patched CNT/MnO_2 nanocomposite papers for the electrode of high-performance flexible asymmetric supercapacitors," ACS Appl. Mater. Interfaces **5**, 3408–3416 (2013).
[25] D. Gueon and J. H. Moon, "MnO_2 nanoflake-shelled carbon nanotube particles for high-performance supercapacitors," ACS Sustainable Chem. Eng. **5**, 2445–2453 (2017).
[26] B. Brown, I. A. Cordova, C. B. Parker, B. R. Stoner, and J. T. Glass, "Optimization of active manganese oxide electrodeposits using graphenated carbon nanotube electrodes for supercapacitors," Chem. Mater. **27**, 2430–2438 (2015).
[27] J. Jiang, Y. Li, J. Liu, X. Huang, C. Yuan, and X. W. D. Lou, "Recent advances in metal oxide-based electrode architecture design for electrochemical energy storage," Adv. Mater. **24**, 5166–5180 (2012).
[28] G. Lota, K. Fic, and E. Frackowiak, "Carbon nanotubes and their composites in electrochemical applications," Energy Environ. Sci. **4**, 1592 (2011).
[29] X. Hu, H. Nan, M. Liu, S. Liu, T. An, and H. Tian, "Battery-like $MnCo_2O_4$ electrode materials combined with active carbon for hybrid supercapacitors," Electrochim. Acta **306**, 599–609 (2019).
[30] H. Tian, X. Lang, H. Nan, P. An, W. Zhang, X. Hu, and J. Zhang, "Nanosheet-assembled $LaMnO_3$@$NiCo_2O_4$ nanoarchitecture growth on Ni foam for high power density supercapacitors," Electrochim. Acta **318**, 651 (2019).
[31] Z. Fan, J. Yan, T. Wei, L. Zhi, G. Ning, T. Li, and F. Wei, "Asymmetric supercapacitors based on graphene/MnO_2 and activated carbon nanofiber electrodes with high power and energy density," Adv. Funct. Mater. **21**, 2366–2375 (2011).

[32]F. Ochai-Ejeh, M. J. Madito, K. Makgopa, M. N. Rantho, O. Olaniyan, and N. Manyala, "Electrochemical performance of hybrid supercapacitor device based on birnessite-type manganese oxide decorated on uncapped carbon nanotubes and porous activated carbon nanostructures," Electrochim. Acta **289**, 363–375 (2018).
[33]L. Deng, G. Zhu, J. Wang, L. Kang, Z.-H. Liu, Z. Yang, and Z. Wang, "Graphene–MnO_2 and graphene asymmetrical electrochemical capacitor with a high energy density in aqueous electrolyte," J. Power Sources **196**, 10782–10787 (2011).
[34]Z.-S. Wu, W. Ren, D.-W. Wang, F. Li, B. Liu, and H.-M. Cheng, "High-energy MnO_2 nanowire/graphene and graphene asymmetric electrochemical capacitors," ACS Nano **4**, 5835–5842 (2010).
[35]H. Gao, F. Xiao, C. B. Ching, and H. Duan, "High-performance asymmetric supercapacitor based on graphene hydrogel and nanostructured MnO_2," ACS Appl. Mater. Interfaces **4**, 2801–2810 (2012).
[36]Y. Shao, H. Wang, Q. Zhang, and Y. Li, "High-performance flexible asymmetric supercapacitors based on 3D porous graphene/MnO_2 nanorod and graphene/Ag hybrid thin-film electrodes," J. Mater. Chem. C **1**, 1245–1251 (2013).
[37]H. Jiang, C. Li, T. Sun, and J. Ma, "A green and high energy density asymmetric supercapacitor based on ultrathin MnO_2 nanostructures and functional mesoporous carbon nanotube electrodes," Nanoscale **4**, 807–812 (2012).
[38]L.-F. Chen, Z.-H. Huang, H.-W. Liang, Q.-F. Guan, and S.-H. Yu, "Bacterial-cellulose-derived carbon nanofiber@MnO_2 and nitrogen-doped carbon nanofiber electrode materials: An asymmetric supercapacitor with high energy and power density," Adv. Mater. **25**, 4746–4752 (2013).
[39]M. Li, Q. Chen, and H. Zhan, "Ultrathin manganese dioxide nanosheets grown on partially unzipped nitrogen-doped carbon nanotubes for high-performance asymmetric supercapacitors," J. Alloys Compd. **702**, 236–243 (2017).
[40]K. Makgopa, P. M. Ejikeme, C. J. Jafta, K. Raju, M. Zeiger, V. Presser, and K. I. Ozoemena, "A high-rate aqueous symmetric pseudocapacitor based on highly graphitized onion-like carbon/birnessite-type manganese oxide nanohybrids," J. Mater. Chem. A **3**, 3480–3490 (2015).
[41]X. Zhang, P. Yu, H. Zhang, D. Zhang, X. Sun, and Y. Ma, "Rapid hydrothermal synthesis of hierarchical nanostructures assembled from ultrathin birnessite-type MnO_2 nanosheets for supercapacitor applications," Electrochim. Acta **89**, 523–529 (2013).
[42]T. Cottineau, M. Toupin, T. Delahaye, T. Brousse, and D. Bélanger, "Nanostructured transition metal oxides for aqueous hybrid electrochemical supercapacitors," Appl. Phys. A **82**, 599–606 (2006).
[43]Q. Qu, P. Zhang, B. Wang, Y. Chen, S. Tian, Y. Wu, and R. Holze, "Electrochemical performance of MnO_2 nanorods in neutral aqueous electrolytes as a cathode for asymmetric supercapacitors," J. Phys. Chem. C **113**, 14020–14027 (2009).
[44]K. Makgopa, K. Raju, P. M. Ejikeme, and K. I. Ozoemena, "High-performance Mn_3O_4/onion-like carbon (OLC) nanohybrid pseudocapacitor: Unravelling the intrinsic properties of OLC against other carbon supports," Carbon **117**, 20–32 (2017).
[45]I. I. Misnon and R. Jose, "Synthesis and electrochemical evaluation of the PANI/δ-MnO_2 electrode for high performing asymmetric supercapacitors," New J. Chem. **41**, 6574–6584 (2017).
[46]V. Khomenko, E. Raymundo-Piñero, and F. Béguin, "Optimisation of an asymmetric manganese oxide/activated carbon capacitor working at 2 V in aqueous medium," J. Power Sources **153**, 183–190 (2006).
[47]J. Fei, J. Zhao, H. Zhang, A. Wang, C. Qin, P. Cai, X. Feng, and J. Li, "One-pot mass self-assembly of MnO_2 sponge-like hierarchical nanostructures through a limited hydrothermal reaction and their environmental applications," J. Colloid Interface Sci. **490**, 621–627 (2017).
[48]B. Akinwolemiwa, C. Peng, and G. Z. Chen, "Redox electrolytes in supercapacitors," J. Electrochem. Soc. **162**, A5054–A5059 (2015).
[49]A. Laheäär, P. Przygocki, Q. Abbas, and F. Béguin, "Appropriate methods for evaluating the efficiency and capacitive behavior of different types of supercapacitors," Electrochem. Commun. **60**, 21–25 (2015).
[50]P. Simon and Y. Gogotsi, "Materials for electrochemical capacitors," Nat. Mater. **7**, 845–854 (2008).
[51]F. O. Ochai-Ejeh, M. J. Madito, D. Y. Momodu, A. A. Khaleed, O. Olaniyan, and N. Manyala, "High performance hybrid supercapacitor device based on cobalt manganese layered double hydroxide and activated carbon derived from cork (quercus suber)," Electrochim. Acta **252**, 41–54 (2017).
[52]C. Mattevi, H. Kim, and M. Chhowalla, "A review of chemical vapour deposition of graphene on copper," J. Mater. Chem. **21**, 3324–3334 (2011).
[53]M. Zhao and H. Song, "Synthesis of carbon-encapsulated iron carbide/iron nanoparticles from phenolic-formaldehyde resin and ferric nitrate," Mater. Chem. Phys. **124**, 861–864 (2010).
[54]T. K. Gupta, B. P. Singh, V. N. Singh, S. Teotia, A. P. Singh, I. Elizabeth, S. R. Dhakate, S. K. Dhawan, and R. B. Mathur, "MnO_2 decorated graphene nanoribbons with superior permittivity and excellent microwave shielding properties," J. Mater. Chem. A **2**, 4256–4263 (2014).
[55]C. Röder, T. Weißbach, C. Himcinschi, J. Kortus, S. Dudczig, and C. G. Aneziris, "Raman spectroscopic characterization of novel carbon-bonded filter compositions for steel melt filtration," J. Raman Spectrosc. **45**, 128–132 (2014).
[56]J. Zhang, C. Liu, and G. Shi, "Raman spectroscopic study on the structural changes of polyaniline during heating and cooling processes," J. Appl. Polym. Sci. **96**, 732–739 (2005).
[57]M. Sawangphruk, M. Suksomboon, K. Kongsupornsak, J. Khuntilo, P. Srimuk, Y. Sanguansak, P. Klunbud, P. Suktha, and P. Chiochan, "High-performance supercapacitors based on silver nanoparticle-polyaniline-graphene nanocomposites coated on flexible carbon fiber paper," J. Mater. Chem. A **1**, 9630–9636 (2013).
[58]C. Avril, V. Malavergne, R. Caracas, B. Zanda, B. Reynard, E. Charon, E. Bobocioiu, F. Brunet, S. Borensztajn, S. Pont, M. Tarrida, and F. Guyot, "Raman spectroscopic properties and Raman identification of CaS-MgS-MnS-FeS-Cr_2FeS_4 sulfides in meteorites and reduced sulfur-rich systems," Meteorit. Planet. Sci. **48**, 1415–1426 (2013).
[59]J.-A. Bourdoiseau, M. Jeannin, R. Sabot, C. Rémazeilles, and P. Refait, "Characterisation of mackinawite by Raman spectroscopy: Effects of crystallisation, drying and oxidation," Corros. Sci. **50**, 3247–3255 (2008).
[60]E. B. Hansson, M. S. Odziemkowski, and R. W. Gillham, "Formation of poorly crystalline iron monosulfides: Surface redox reactions on high purity iron, spectroelectrochemical studies," Corros. Sci. **48**, 3767–3783 (2006).
[61]P. Colomban, S. Cherifi, and G. Despert, "Raman identification of corrosion products on automotive galvanized steel sheets," J. Raman Spectrosc. **39**, 881–886 (2008).
[62]X. Yang, C. Li, J. Huang, Y. Liu, W. Chen, J. Shen, Y. Zhu, and C. Li, "Nitrogen-doped Fe_3C@C particles as an efficient heterogeneous photo-assisted fenton catalyst," RSC Adv. **7**, 15168–15175 (2017).
[63]M. K. Nieuwoudt, J. D. Comins, and I. Cukrowski, "The growth of the passive film on iron in 0.05M NaOH studied *in situ* by Raman micro-spectroscopy and electrochemical polarisation. Part I: Near-resonance enhancement of the Raman spectra of iron oxide and oxyhydroxide compounds," J. Raman Spectrosc. **42**, 1335–1339 (2011).
[64]N. M. Ndiaye, B. D. Ngom, N. F. Sylla, T. M. Masikhwa, M. J. Madito, D. Momodu, T. Ntsoane, and N. Manyala, "Three dimensional vanadium pentoxide/graphene foam composite as positive electrode for high performance asymmetric electrochemical supercapacitor," J. Colloid Interface Sci. **532**, 395–406 (2018).
[65]X. Feng, Z. Yan, N. Chen, Y. Zhang, X. Liu, Y. Ma, X. Yang, and W. Hou, "Synthesis of a graphene/polyaniline/MCM-41 nanocomposite and its application as a supercapacitor," New J. Chem. **37**, 2203 (2013).
[66]S. K. Lai, C. M. Luk, L. Tang, K. S. Teng, and S. P. Lau, "Photoresponse of polyaniline-functionalized graphene quantum dots," Nanoscale **7**, 5338–5343 (2015).
[67]M. V. Morales-Gallardo, A. M. Ayala, M. Pal, M. A. Cortes Jacome, J. A. Toledo Antonio, and N. R. Mathews, "Synthesis of pyrite FeS_2 nanorods by simple hydrothermal method and its photocatalytic activity," Chem. Phys. Lett. **660**, 93–98 (2016).
[68]G. H. Le, A. Q. Ha, Q. K. Nguyen, K. T. Nguyen, P. T. Dang, H. T. K. Tran, L. D. Vu, T. V. Nguyen, G. D. Lee, and T. A. Vu, "Removal of Cd^{2+} and Cu^{2+} ions from aqueous solution by using Fe–Fe_3O_4/graphene oxide as a novel and efficient adsorbent," Mater. Res. Express **3**, 105603 (2016).

[69]G. Wu, C. M. Johnston, N. H. Mack, K. Artyushkova, M. Ferrandon, M. Nelson, J. S. Lezama-Pacheco, S. D. Conradson, K. L. More, D. J. Myers, and P. Zelenay, "Synthesis–structure–performance correlation for polyaniline–Me–C non-precious metal cathode catalysts for oxygenreduction in fuelcells," J. Mater. Chem. **21**, 11392–11405 (2011).
[70]Y. Luo, D. Kong, Y. Jia, J. Luo, Y. Lu, D. Zhang, K. Qiu, C. M. Li, and T. Yu, "Self-assembled graphene@PANI nanoworm composites with enhanced supercapacitor performance," RSC Adv. **3**, 5851–5859 (2013).
[71]Y. Zhou, H. Xu, N. Lachman, M. Ghaffari, S. Wu, Y. Liu, A. Ugur, K. K. Gleason, B. L. Wardle, and Q. M. Zhang, "Advanced asymmetric supercapacitor based on conducting polymer and aligned carbon nanotubes with controlled nanomorphology," Nano Energy **9**, 176–185 (2014).
[72]W. Sun and X. Chen, "Preparation and characterization of polypyrrole films for three-dimensional micro supercapacitor," J. Power Sources **193**, 924–929 (2009).
[73]H. Li, J. Wang, Q. Chu, Z. Wang, F. Zhang, and S. Wang, "Theoretical and experimental specific capacitance of polyaniline in sulfuric acid," J. Power Sources **190**, 578–586 (2009).